Comparison of self-consistent simulations with observed magnetic field and ion plasma parameters in the ring current during the 10 August 2000 magnetic storm

Margaret W. Chen,[1] Colby L. Lemon,[1] Timothy B. Guild,[1] Michael Schulz,[2] James L. Roeder,[1] and Guan Le[3]

[1]   We assess whether magnetically and electrically self-consistent ring current simulations can account simultaneously for in situ magnetic field and ion flux measurements in the inner magnetosphere during the large 10 August 2000 storm (min $Dst = -107$ nT). We use the Rice Convection Model–Equilibrium (RCM-E) and drive it with time-dependent magnetic field, electric field, and plasma boundary conditions that are guided by empirical and assimilative models. Comparisons of the simulated and observed magnetic field from Geostationary Operational Environmental Satellites (GOES) and observed proton differential flux spectra from Los Alamos National Laboratory (LANL) satellites are made at geosynchronous orbit (GEO). Similarly, simulated and observed magnetic field and proton density and temperature are compared along the orbit of Polar ($r \sim 1.8$–9 R_E) for the event. The simulated and observed magnetic field components agree reasonably well at GEO and along the orbit of Polar. However, since the effects of substorm dipolarizations are not explicitly modeled, the simulation fails to reproduce observed sawtooth fluctuations in the magnetic field. Over energies from 1 to 150 keV, the RCM-E reproduced well the ion dispersion features in the LANL 1994-084 ion differential flux spectra over energies at GEO and proton densities and temperatures calculated from Polar proton flux measurements. Thus, the RCM-E simulations can account simultaneously for in situ magnetic field and ion flux measurements for the 10 August 2000 storm. This demonstrates that a self-consistent model can produce realistic features of the storm time inner magnetosphere.

1.   Introduction

[2]   The ring current, consisting of ions and electrons with energies $\sim$10 to 200 keV [e.g., *Frank*, 1967; *Williams*, 1981] that partially or entirely encircle the Earth, can cause major perturbations in the geomagnetic field during magnetic storms. Indeed, large equatorial magnetic field depressions (~-100 to -200 nT) at $L \sim 3$ to 4 have been measured during the main phases of storms [*Cahill*, 1966; *Wygant et al.*, 1998]. Simulations [*Chen et al.*, 2005, 2006] have also shown storm-time magnetic field perturbations associated with the ring current in localized regions at $L \sim 3$ to 4 that can be comparable to half the dipole's equatorial intensity there. Thus, taking proper account of the ring current field in the simulation can significantly affect the transport and loss of inner magnetospheric particles. In other words, the storm time particle transport needs to be calculated self-consistently with the magnetic and electric fields.

[3]   When thus simulated self-consistently with the equilibrium version (RCM-E) of the Rice Convection Model–Equilibrium (RCM-E) [*Lemon et al.*, 2004], the ring current turns out to be significantly weaker than when simulated without requiring the magnetic and electric fields to be consistent with each other and with the resulting particle transport. The main reason for this is that charged particles in the hot plasma are less efficiently energized by inward magnetic field intensity into which they are transported. Moreover, magnetic field lines become stretched outward (thereby generating an induced electric field that impedes particle

[1]Space Science Applications Laboratory, The Aerospace Corporation, El Segundo, California, USA.
[2]Retired from Lockheed-Martin Advanced Technology Center, Palo Alto, California, USA.
[3]NASA Goddard Space Flight Center, Greenbelt, Maryland, USA.

Corresponding author: M. W. Chen, Space Science Applications Laboratory, The Aerospace Corporation, MS M2-260, PO Box 92957, El Segundo, CA 90009, USA. (margaret.w.chen@aero.org)
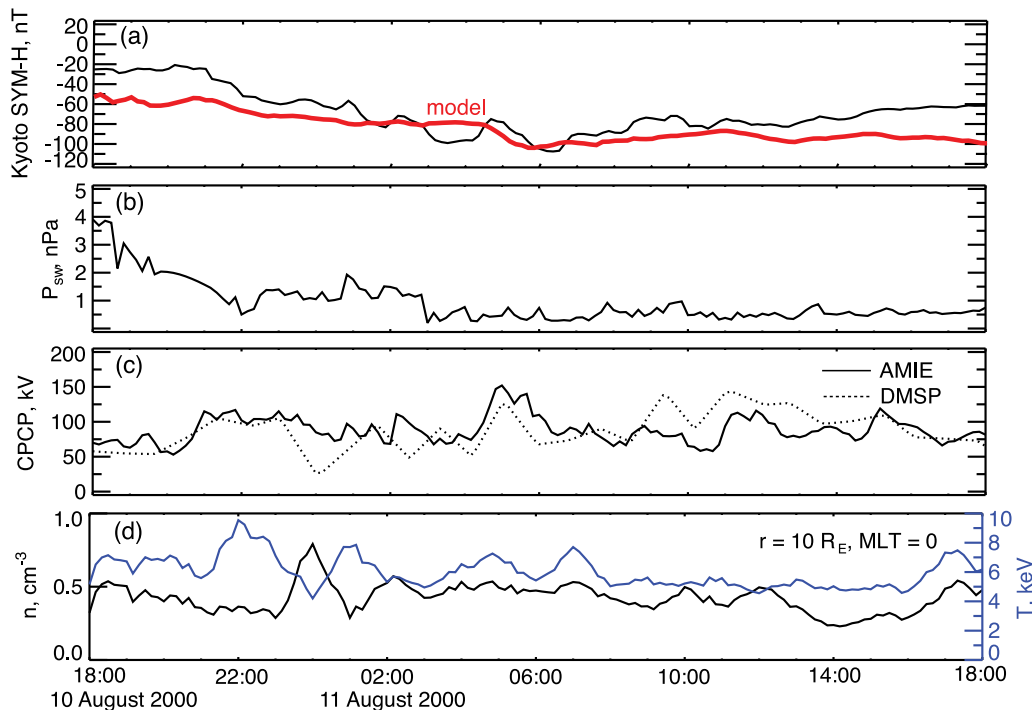
Figure 1. (a) Time trace of Kyoto *SYM-H* (black curve) and the simulated *Dst* calculated from the Dessler-Parker-Sckopke relation (red curve), (b) the solar wind pressure from CDAWeb, (c) the cross-polar cap potential from the AMIE model from the Space Weather Re-analysis Project (black curve) and from DMSP drift meter data (dotted curve), and (d) the ion density (blue curve) and ion temperature (black curve) at the boundary of the RCM-E simulation at a radial distance of 10 R_E at midnight.

access) as a result of such inward transport. Plasma pressure and magnetic field perturbations in the inner magnetosphere are thus considerably smaller when the simulation of particle transport is treated in a self-consistent way rather than not [cf. *Liu et al.*, 2006; *Zaharia et al.*, 2006; *Chen et al.*, 2006], and the ring current's simulated magnetic contribution to the pressure-corrected *Dst** index [*de Gonzalez and Gonzalez*, 1998; *Liemohn et al.*, 2001] is significantly reduced. *Chen et al.* [2006], for example, found that the ring current's contribution to *Dst** for a large storm event was reduced by ~25% during a representative storm's main phase when magnetic self-consistency was invoked. Thus, ring current simulations that do not self-consistently treat the ring current and the magnetospheric configuration tend to overestimate the overall ring current intensity. However, since *Dst* is a ground-based index that includes effects from ionospheric, magnetopause, tail, and ground-induced currents, in situ magnetic intensities and particle fluxes in the ring current region are arguably more direct measurements of ring current intensity than *Dst* itself is.

[4] The ring current strength is affected by variations in the plasma sheet (source) population also. For example, in simulations that were admittedly not self-consistent, *Chen et al.* [1994], *Kozyra et al.* [1998], *Liemohn et al.* [2001], and *Lavraud and Jordanova* [2007] have shown that a superdense plasma sheet associated with high solar wind ion density [*Borovsky et al.*, 1997] can lead to a strong ring current. Furthermore, the solar wind influence on plasma sheet conditions can also affect local time asymmetries as

the ring current develops [*Chen et al.*, 2007]. Thus, it is important to specify realistic time-dependent plasma source populations for ring current simulations.

[5] In this study we use the self-consistent RCM-E to simulate the large 10 August 2000 storm. The black curve in Figure 1a shows the time trace of the Kyoto *SYM-H* index for this storm. The min *SYM-H* = −107 nT is attained after an approximately 10 h main phase. We chose this storm event because of the good availability of in situ magnetic field data from NOAA's Geostationary Operational Environmental Satellite (GOES 8 and 10) and NASA's Polar satellite as well as ion flux data from Polar and from the Los Alamos National Laboratory's (LANL) satellites. By making detailed model-data comparisons of the magnetic intensity and ion flux spectra or ion plasma properties in the inner magnetosphere, we assess whether self-consistent simulations can account for observed storm time magnetic intensities and ion fluxes simultaneously. While there have been many previous simulation studies that accounted for storm time enhancement of ion fluxes over ring current energies using either nonself-consistent models [e.g., *Fok et al.*, 1996; *Jordanova et al.*, 1998, 2006] or magnetically self-consistent models [*Chen et al.*, 2006], very few [e.g., *Zaharia et al.*, 2010; *Yu et al.*, 2012] have attempted to account simultaneously for the observed ion distributions and the magnetic field. The ability to reproduce the ring current particle distribution and the magnetic field simultaneously is a more rigorous test of how well one can simulate

the important physical processes associated with the formation of the ring current.

2. Description of Simulation Model and Its Boundary Conditions

2.1. Rice Convection Model–Equilibrium

[6] The Rice Convection Model (RCM) [*Toffoletto et al.*, 2003, and references therein] computes the bounce-averaged guiding center drift motion of isotropic ion and electron distributions (as if particles of any energy were permanently subject to strong pitch angle diffusion) across closed field lines in the magnetosphere, the Birkeland currents that result from the divergence of particle drift currents, and the electric fields that self-consistently satisfy Ohm's law (given an ionospheric conductivity model and the computed Birkeland currents). Ion charge exchange and electron loss at a uniform fraction (=1/3) of the loss rate for strong pitch angle scattering (equivalent to a backscatter fraction of 2/3) are included. The RCM takes the magnetic field, traditionally provided by semiempirical models, electric potentials in the ionosphere, and plasma boundary distributions as inputs.

[7] In place of a semiempirical magnetic field model, the Rice Convection Model–Equilibrium (RCM-E) uses an equilibrium magnetic field solver to evolve the magnetic field self-consistently with the RCM plasma [*Lemon et al.*, 2003, 2004; *Lemon*, 2005]. The combined model therefore simulates the full energy-dependent particle drifts (still assuming isotropy in pitch angle) along with the self-consistent evolution of the electric *and* magnetic fields in the magnetospheric region of closed magnetic field lines. The RCM-E has been used to model the physics of the substorm growth phase [*Toffoletto et al.*, 2001; *Lemon*, 2005] and expansion phase [*Toffoletto et al.*, 2000], steady magnetospheric convection [*Lemon*, 2005; *Yang et al.*, 2010], and the process of ring current injection [*Lemon et al.*, 2004].

2.2. Time-Dependent Boundary Conditions for RCM-E Simulation of 10 August 2000 Storm Event

[8] To simulate the inner magnetosphere and plasma sheet, we drive the model with boundary conditions that vary as realistically as possible. The primary inputs to the RCM-E are the electric potential and magnetic field at the outer boundary of the model, the plasma distribution on this outer boundary for each species, and the ionospheric conductance pattern. For the present study the boundary conditions are updated every ten minutes. The outer boundary of the RCM-E is a magnetic surface that reaches out to an equatorial radius of 13 R_E or to the equatorial magnetopause, whichever is nearer to the geocenter. The time-dependent magnetic field boundary conditions are specified by the empirical model of *Tsyganenko and Sitnov* [2005] (TS04), which is driven by upstream data from combined ACE and Wind (obtained from NASA's OMNIWeb Plus database). Figure 1b shows the solar wind pressure P_{sw} during the storm of 10 August 2000. The solar wind pressure decreased slightly during the early main phase and remained below 3.5 nPa for the rest of the time period shown. The magnetopause standoff distance contracts and expands in response to such solar wind pressure variations, and these changes are reflected in our specified boundary conditions. Such changes in the magnetic field lead to particle transport and

energization driven by induced electric fields, which are accounted for through conservation of the appropriate adiabatic invariant in the RCM-E. In the RCM-E, the effects of induced electric fields are handled by tracking the magnetic field mapping from a stationary grid of ionospheric points (where the magnetic field is assumed to be constant in time) to points in the magnetosphere where the magnetic field is changing. Plasma transport across field lines (due to potential electric fields and gradient/curvature drift) is calculated explicitly, while induced electric fields are assumed to move plasma at the same velocity as the field line ("frozen-in flux"). Equatorial plots of plasma quantities are therefore shown on a time-dependent grid that is a distorted mapping of the stationary ionospheric grid. During times of magnetic field stretching, the equatorial grid mapping expands, while localized increases in the magnetic intensity lead the grid mapping to contract. Extreme field line stretching can significantly reduce the equatorial grid resolution, and we therefore use a nonuniform ionospheric grid whose resolution is very high in the auroral zone (approximately 20 points per degree of latitude for storm simulations).

[9] To specify the time-varying boundary conditions on the electric potential, we use the Assimilative Model of Ionospheric Electrodynamics (AMIE) [*Richmond et al.*, 1998] reanalysis of *Kihn and Ridley* [2005] driven by upstream conditions. The AMIE potential drops across the polar cap, shown as the black curve in Figure 1c, resemble the interpolated cross-polar cap potentials inferred from DMSP drift meter data (http://cindispace.utdallas.edu/DMSP/dmsp_data_at_utdallas.html) shown as the black dotted curve in Figure 1c during the 24 h period shown. This lends confidence in the AMIE reanalysis results for the cross-polar cap potential. For this study, we set the polar cap boundary at an equatorial radius $r = 10\ R_E$ in the RCM-E model.

[10] In this study we assume a constant and uniform ionospheric conductance (Hall and Pedersen) of 10 S per hemisphere. We ran the IRI 2007 [*Bilitza and Reinisch*, 2008] model to calculate the conductance values for 10 August 2010. The spatially averaged conductance value was about 8 S. We rounded the value to 10 S to use for uniform conductance. In the future we will specify more realistic ionospheric conductances by using the IRI 2007 empirical model [*Bilitza and Reinisch*, 2008].

[11] During the 10 August 2000 storm, in situ particle measurements in the plasma sheet included data from LANL/Magnetospheric Plasma Analyzer (MPA) [*McComas et al.*, 1993] and Synchronous Orbit Particle Analyzer (SOPA) [*Belian et al.*, 1992] (courtesy of Los Alamos National Laboratory). The MPA instrument measures ions and electrons with energies ∼1 eV to 40 keV, while SOPA measures protons and electrons with energies ∼50 keV to ∼50 MeV and ∼50 keV to 1.6 MeV, respectively. Also available is a reanalysis [*O'Brien and Lemon*, 2007] of LANL/MPA plasma moments for particle energies <40 keV. However, a reanalysis of moments that combine the lower-energy MPA and high-energy SOPA data is not currently available. Moreover, NASA's Geotail satellite was not in the plasma sheet during the event of interest. We use the available in situ plasma sheet measurements or plasma moment reanalysis to help specify our outer plasma boundary conditions, taken to be at a geocentric radial distance $r = 10\ R_E$, spaced every 0.25 h in magnetic local time (MLT). We

choose 10 R_E rather than 6.6 R_E for the outer boundary because we wish to use geosynchronous observations to make comparisons with our simulation results. We note that we choose the plasma boundary to be at $r = 10\ R_E$, which is within the outer boundary of the RCM-E (equatorial radius of 13 R_E or to the equatorial magnetopause as explained above). We set the plasma boundary inside the magnetic field boundary because, in general, this leads to better force balance between the plasma and magnetic field.

[12] In view of results found by *Christon et al.* [1991] from analysis of ISEE 1 measurements in the central plasma sheet during disturbed times, we assume kappa ion and electron distributions at the outer plasma boundary ($r = 10\ R_E$):

$$f(E) = \left[1 + \left(\frac{E}{\kappa E_0}\right)\right]^{-\kappa - 1} f(0), \tag{1}$$

where E is the kinetic energy of an individual particle and E_0 is a characteristic energy for the distribution. Since our simulations in this work are nonrelativistic, we take $E = p^2/2m_0$ for a particle of scalar momentum p and rest mass m_0. We thereby calculate from (1) the plasma density

$$N = 4\pi f(0) \int_0^\infty \left[1 + \left(\frac{E}{\kappa E_0}\right)\right]^{-\kappa - 1} p^2 dp$$
$$= 2\pi (2m_0 \kappa E_0)^{\frac{3}{2}} f(0) \left[\frac{\Gamma(1.5)\Gamma(\kappa - 0.5)}{\Gamma(\kappa + 1)}\right], \tag{2}$$

where the mean energy

$$\langle E \rangle = \left(\frac{2\pi}{m_0}\right) f(0) \int_0^\infty \left[1 + \left(\frac{E}{\kappa E_0}\right)\right]^{-\kappa - 1} p^4 dp = \frac{3\kappa E_0}{2\kappa - 3} \tag{3}$$

by using equation (3.2414) of *Gradshteyn and Ryzhik* [1980]. The limit $\kappa \to \infty$ thus yields the well known result that $\langle E \rangle = (3/2)\ E_0$ for a Maxwellian distribution.

[13] We specify a time-varying but MLT-independent kappa parameter at the boundary by making power law fits to the high-energy tail of the LANL/SOPA phase-space distributions at geosynchronous altitude. We admit that this procedure yields only a rough estimate of the kappa parameter but (given the scarcity of data) we have little choice. Also, a power law distribution is expected to remain self-similar (with the same exponent) under radial transport [*Nakada et al.*, 1965].

[14] To map the characteristic energy E_0 in (1) from equatorial $r = 6.6\ R_E$ to equatorial $r = 10\ R_E$, we assume that E_0 varies inversely as the 2/3 power of flux tube volume

$$\Psi = \oint \frac{ds}{B}, \tag{4}$$

where ds is the element of arc length along a field line, so as to conserve the adiabatically invariant quantity $\lambda = \Psi^{2/3}E$ in the RCM-E for each representative particle. This is analogous to the suggestion of *Nakada et al.* [1965] that the characteristic energy of an exponential spectrum "should" vary as the energy of an individual particle conserving its first two adiabatic invariants.

[15] We infer the values of E_0 in (1) at equatorial $r = 6.6\ R_E$ for available MLT values φ primarily by using reanalyzed LANL/MPA data, for which the mean energies and partial pressures corresponding to particle energies $E < 40$ keV are available. Since mean energies and partial pressures from reanalyzed LANL/MPA and SOPA data are not available, we have assumed that the mean energy inferred from LANL/MPA data is about half the total that would have been inferred from the full range of particle energies (i.e., from including LANL/SOPA data for $E \gtrsim 50$ keV). Thus, we assume that the reported partial pressure from reanalysis of LANL/MPA data accounts for approximately half of the total plasma pressure at equatorial $r = 6.6\ R_E$. We have successfully tested this assumed extrapolation against available LANL/SOPA data in a few instances.

[16] As we have mentioned above, we treat the boundary values of κ, E_0, and $f(0)$ ion (1) as being independent of MLT at equatorial $r = 10\ R_E$ because we lack sufficient MLT coverage from Polar, MPA, and SOPA to model the boundary condition on $f(E, t)$ any better than this. In order to make the corresponding mappings definite, we interpolate available geosynchronous data to magnetic midnight ($\varphi = 0$) and then extrapolate E_0 to equatorial $r = 10\ R_E$ by invoking the conservation of $\lambda_0 \equiv E_0 \Psi^{2/3}$ along the corresponding (time-reversed) drift trajectory. However, we do not know a priori what the drift trajectories will be (because of the feedback between plasma and fields), so we choose simply to map along the midnight meridian from $r = 6.6\ R_E$ to $r = 10\ R_E$, and then apply the resulting plasma condition uniformly around the outer boundary. As part of this process, we assume that plasma flux tube content ($n\Psi$) is a factor of two higher at $r = 10\ R_E$, since only a fraction of the convection electric field at 10 R_E penetrates to 6.6 R_E. Strictly speaking, it should also be true that gradient/curvature drift preferentially excludes some high-energy particles from penetrating to 6.6 R_E; to the extent that this is true, we lump that together with the assumption that the mean energy obtained from MPA is "approximately half" of the mean energy of the full MPA/SOPA spectrum, and specify λ_0 of plasma at $r = 10\ R_E$ to be exactly twice the value of λ_0 inferred from MPA data at $r = 6.6\ R_E$. Because our boundary conditions on the electrostatic potential lead to outflow on the dayside, the plasma boundary condition there does not significantly impact our simulations.

[17] The black and blue curves in Figure 1d show examples of the variation of the ion density and temperature at $r = 10\ R_E$ and at midnight on the boundary. From Figure 1d, one can see that the ion density and temperature boundary conditions at $r = 10\ R_E$ and midnight do not vary rapidly. Because of this, and the fact that these values likely have large uncertainties, we choose not to apply any time lag for plasma parameters between $r = 10\ R_E$ and 6.6 R_E. Our plasma boundary conditions are rough approximations, but we believe our technique is reasonable given the limited (geosynchronous) plasma sheet data available. We also believe that more sophisticated techniques for estimating our plasma boundary conditions would not significantly reduce the uncertainty in their values. Furthermore, because our boundary conditions are so loosely based on geosynchronous data, and only at midnight, we believe it allows us to make comparisons of the model results with geosynchronous data
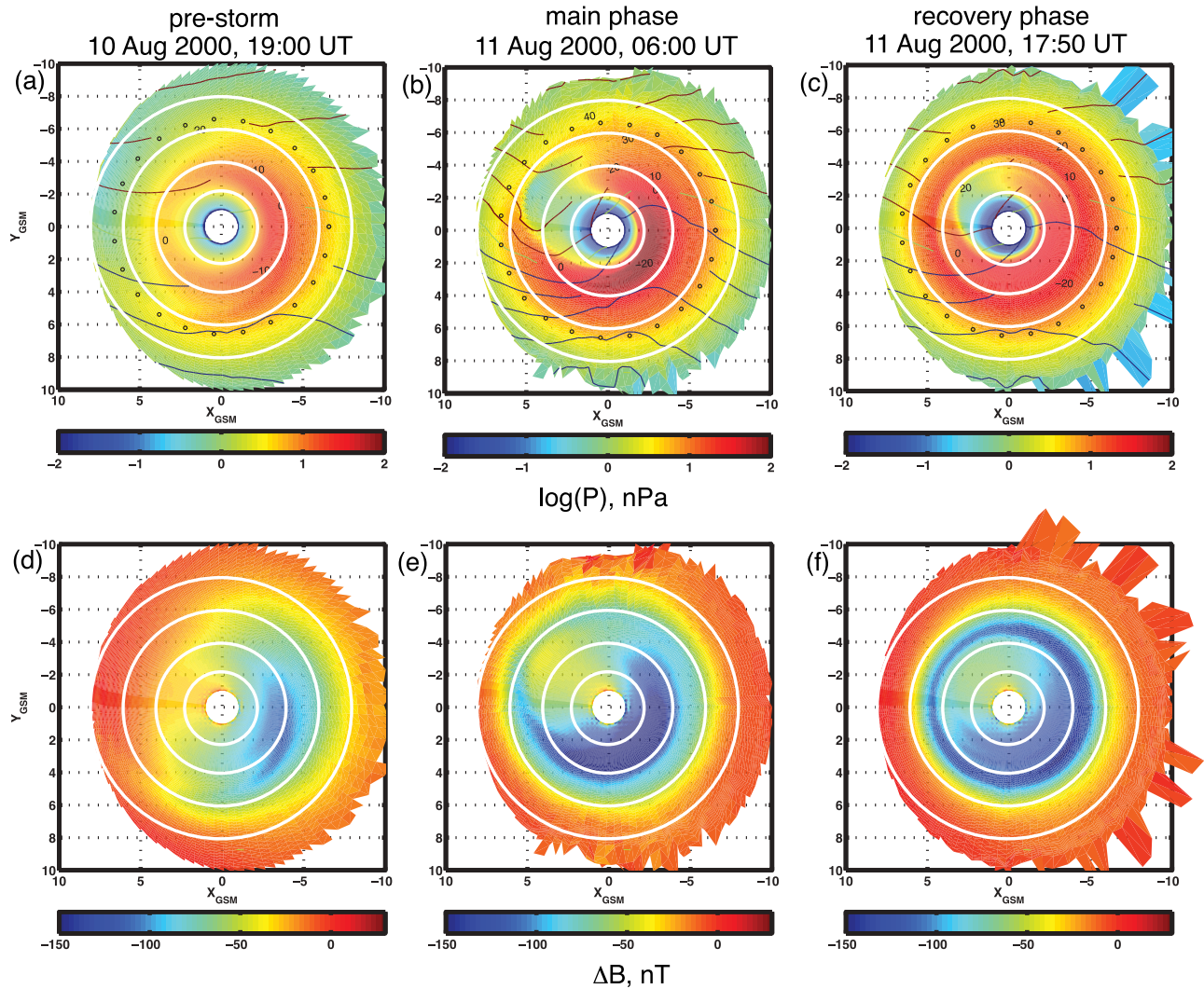
Figure 2. (a–c) The simulated equatorial plasma pressure (total of ions and electrons). Equipotential contours in units of kV are plotted over the pressure plots. Concentric circles spaced two Earth radii apart are shown in white. The small black open circles represent the geosynchronous orbit. (d–f) The simulated magnetic perturbation during the prestorm (Figures 2a and 2d), main phase (Figures 2b and 2e), and recovery phase of the storm event (Figures 2c and 2f).

without unduly influencing the outcome at magnetic local times other than midnight.

## 3. Summary of Simulation Results

[18] Using the time-dependent boundary conditions described in section 2, we ran the RCM-E simulation. The red curve in Figure 1a shows the simulated *Dst* index obtained from the Dessler-Parker-Sckopke (DPS) relation [*Dessler and Parker*, 1959; *Sckopke*, 1966]. Agreement between the simulated and the observed *Dst* index (black curve) is reasonable during the storm main phase and early recovery phase (10 August 2000, 22:00 UT to 11 August 2000, 12:00 UT) considering that the DPS relation is a simplistic estimate of *Dst* [*Liemohn*, 2003] during storms. This signifies that the increase in the simulated proton ring current energy content is consistent with the observed

decrease in *Dst* during the storm main phase and early recovery phase.

[19] The simulated equatorial particle pressure for representative times during the storm event are shown in Figures 2a–2c. At a prestorm time of 19:00 UT on 10 August 2000, Figure 2a shows that for a given equatorial radial distance that the pressure tends to be larger on the night side rather than the dayside. By 06:00 UT on 11 August 2000 at a time near the minimum *Dst* value, the overall pressure (see Figure 2b) is more intense than during prestorm and the peak pressure occurs closer to Earth. By 17:50 UT on 11 August 2000 during the recovery phase, the peak pressure (see Figure 2c) occurs farther from Earth and is less intense than at 06:00 UT.

[20] The ring current associated magnetic perturbations in the equatorial plane during representative storm times are shown in Figures 2d–2f. The simulated magnetic perturbation is calculated by subtracting the dipole intensity from the
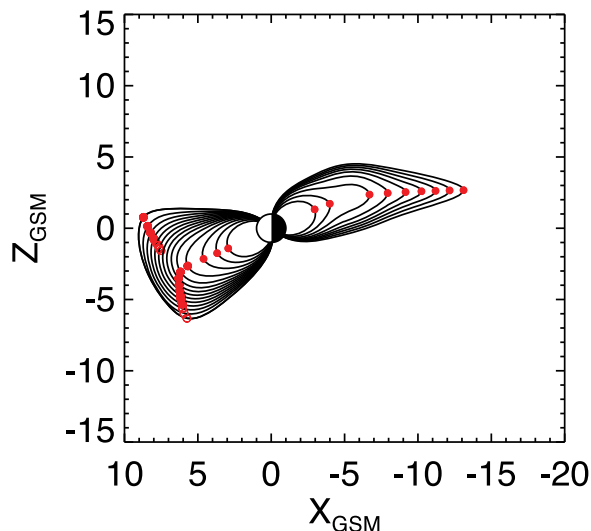
Figure 3. Representative closed magnetic field lines (black curves) in the noon-midnight meridian plane, in the T01 model, the true minimum magnetic intensity on the field line (solid red circles), and the secondary local minima (open red circles) in the magnetic intensity on the bifurcated portion of the minimum B surface.

simulated magnetic intensity. From Figure 2d, the equatorial magnetic perturbation is negative on the night side before the storm. At 06:00 UT on 11 August 2000, Figure 2e shows that there are large ($\Delta B < -100$ nT) magnetic depressions from postnoon to postmidnight in the inner magnetosphere. During the recovery phase at 17:50 UT on August 2000 (see Figure 2f), the peak magnetic depression occurs farther from Earth than at 06:00 UT (see Figure 2e). These representative plots of the total pressure and magnetic depressions in the equatorial plane give an overview of the development of the ring current during the storm.

4. Data-Simulation Comparisons

4.1. Association of Observed Locations in RCM-E

[21] In order to compare our simulation results with observational measurements, we must find a way to associate any point of observation in the real magnetosphere with a physically corresponding point in the RCM-E, which currently does not account for the Earth's magnetic dipole tilt. Our concept is to look for a model point separated by the same amount of latitude from the magnetic equatorial surface (locus of relative minima in B along field lines) as the point of observation. The minimum B surface in the RCM-E lies in the $Z_{GSM} = 0$ plane except for a dayside bifurcation [*Mead*, 1964; *Shabansky*, 1971] at equatorial geocentric distances $r \geq 8$ R_E. The minimum B surface in the real magnetosphere is additionally warped relative to the tilted dipole's equatorial plane by the magnetic effects of magnetopause and cross-tail currents, as well as by the effects of higher multipoles (quadrupole, octupole, etc.) in the Earth's main B field. The plasma sheet and ring current typically span the minimum B surface and may somewhat modify its geometrical configuration.

[22] Except for the noted influence of magnetopause currents, tail currents, and higher multipoles of the Earth's main

magnetic field, we might expect a satisfactory comparison of data with RCM-E output at the same geocentric radial distance r, the same magnetic latitude Λ relative to the dipole's equatorial plane, and the same magnetic local time ϕ (MAG coordinates, as described by *Russell* [1971]). However, it is clear from Figure 3 here that effects of magnetopause and tail currents are not negligible at $r > 6$ R_E in the present context, and from Figure 1 of *Roederer et al.* [1973] that higher harmonics of the Earth's main B field are probably not negligible in the present context at $r < 3$ R_E. (The latter was a contour plot of "elevation" contours for the minimum B surface of the Earth's main magnetic field relative to the dipole's equatorial plane, showing "elevations" varying with longitude by up to ± 0.1 R_E at $r \sim 3$ R_E and by even larger amounts at smaller values of r.)

[23] Accordingly, we have decided to associate any point of observational measurement in the real magnetosphere with a point having the same geocentric radial distance r, the same MLT, and the same latitudinal separation $\tilde{\Lambda} \equiv \Lambda - \Lambda_0$ from the minimum B surface at those values of r and ϕ in the RCM-E. We use the T01 model of *Tsyganenko* [2002a, 2002b] to specify the magnetic latitude Λ_0 of the minimum B surface at the desired values of r and ϕ.

[24] Starting at $\Lambda = 0$ there, we step along the local magnetic field line to locate (in Λ) its minimum value of B. We use this value of Λ (but again with the desired values of r and ϕ) as our next guess at Λ_0 and proceed iteratively until we have identified the correct value of Λ_0 on the minimum B surface to sufficient precision at the desired values of r and ϕ. Finally we calculate the latitudinal separation $\tilde{\Lambda}$ ($=\Lambda - \Lambda_0$) of the measurement site from the minimum B surface in the T01 model at the desired values of r and ϕ. This algorithmic procedure determines the latitude Λ ($=\tilde{\Lambda}$, since $\Lambda_0 = 0$ in the RCM-E) of the point in the RCM-E with which we associate the measurement of interest in the real magnetosphere.

[25] The above procedure for comparing data with simulation results seems to work well as long as we avoid (as we do in this study) the bifurcated portion of the minimum B surface near the dayside magnetopause. No such difficulty is encountered along closed field lines on the night side.

[26] The black curves in Figure 3 illustrate representative closed field lines, as projected onto the noon-midnight meridional plane, in the T01 model for 10 August 2000 at 18:00 UT. (Projection is necessary here because the Earth's main B field is represented by the IGRF 2000.0 rather than by a tilted dipole only.) The red circles show the locations of true minima in B along these field lines. The open red circles correspond to secondary local minima in B on the bifurcated portion of the minimum B surface.

4.2. Comparisons at Geosynchronous Altitude

[27] First, we compare available magnetic field data from the GOES-8 satellite at geosynchronous altitude (GEO) with corresponding simulated RCM-E magnetic field values. The squares in Figure 4 show 10 min averages of the GOES-8 magnetic intensity (Figure 4a), B_x (Figure 4b), B_y (Figure 4c), and B_z (Figure 4d). For reference, Figure 4e shows the dipole tilt (purple curve) and the *SYM-H* index (black curve). The magnetic intensity measured by GOES-8 varied from 91 nT to 146 nT over the time period shown.
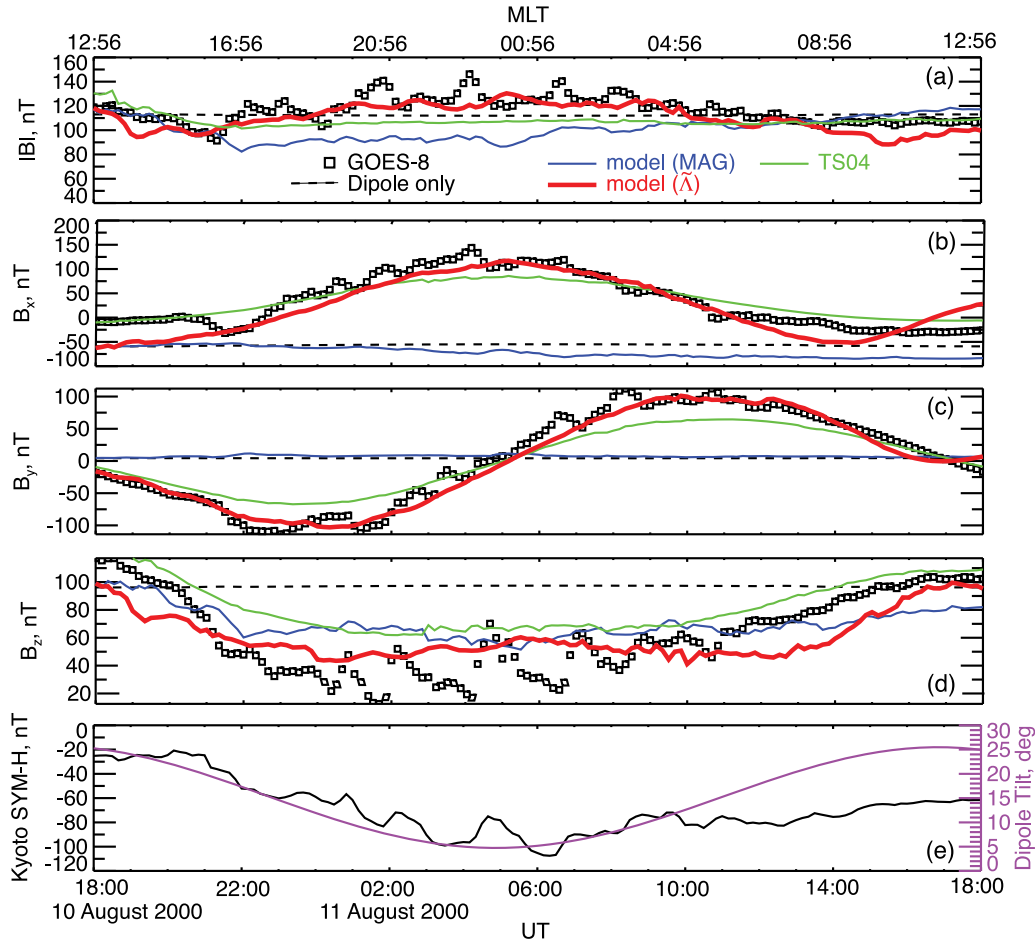
Figure 4. Time traces of the (a) magnetic intensity, (b) B_x, (c) B_y, and (d) B_z. Ten minute averages of GOES-8 data (black squares), a dipole field (dashed curve), the RCM-E quantities in MAG coordinates (blue curve), the RCM-E quantities in $\tilde{\Lambda}$ coordinates (red curve), and the TS04 model (green curve) are shown. (e) The Kyoto *SYM-H* index (black curve) and the dipole tilt (purple curve).

[28] The 10–11 August 2000 storm included sawtooth events, identified as large-amplitude quasiperiodic modulations of the energetic electron and ion fluxes at GEO. *Henderson et al.* [2006] examined in detail these sawtooth events at 23:02 UT, 10 August 2000, 00:41 UT, 01:51 UT, 04:13 UT, 06:39 UT, 08:18 UT, 10:30 UT, and 13:30 UT, 11 August 2000. Fluctuations in all the components of B and |B| at these times are apparent in the GOES-8 data. In this study we are not explicitly modeling substorm dipolarizations that *Henderson et al.* [2006] reported as being associated with sawtooth events. Thus, we do not expect to reproduce magnetic field fluctuations associated with sawtooth events. In Figures 4a–4d, the black dashed curve corresponds to the strength of the dipole magnetic field in MAG coordinates. The constant dipole intensity obviously does not reproduce well the GOES-8 magnetic intensity or its components. The RCM-E magnetic field evaluated at the spacecraft location in MAG coordinates are shown as the blue curves. The blue curve does not reproduce well the B_x or B_y coordinate or the magnetic intensity, but does better in accounting for B_z. The red curves correspond to the RCM-E magnetic field evaluated in the spacecraft $\hat{\Lambda}$ coordinates transformed described in section 4.1. The RCM-E magnetic

intensity and components evaluated at the spacecraft location in $\tilde{\Lambda}$ coordinates agree reasonably well with the GOES-8 data. However, as expected, the simulated magnetic field does not reproduce the fluctuations associated with the sawtooth events or substorm dipolarizations. Finally, the green curves correspond to the TS04 magnetic field model. Sometimes the TS04 magnetic field agrees better with the GOES-8 data; at other times the RCM-E magnetic field in $\tilde{\Lambda}$ coordinates agrees better with the GOES-8 data. From about 21:00 UT on 10 August 2000 to 13:50 UT on 11 August 2000 (main phase and early recovery phase), the RCM-E |B| in $\tilde{\Lambda}$ coordinates agrees better with the GOES-8 data than the TS04 |B| agrees with GOES-8 data.

[29] Next, we compare the observed and simulated omnidirectional ion differential fluxes at GEO. Figure 5a shows a spectrogram of ion differential flux from LANL 1994-084. The spectra at magnetic local times of 00:50 MLT to ∼05:10 MLT are consistent with direct access of plasma from the night side over the full energy range displayed. A dispersion feature in the observed ion differential flux spectrogram starts at ∼05:10 MLT or 22:20 UT. The ion dispersion feature is a signature of an energy-dependent boundary between higher fluxes associated with direct access of plasma
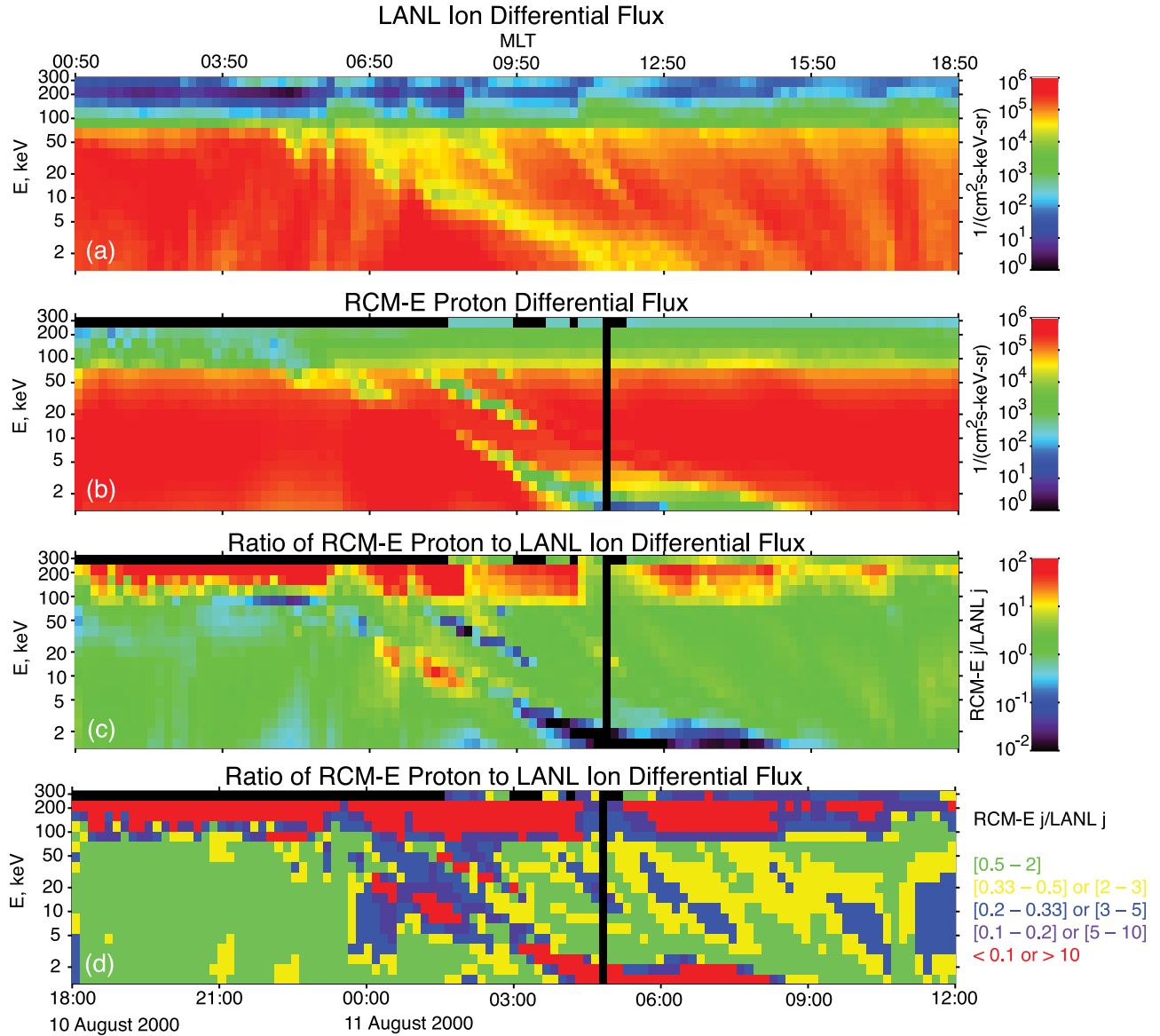
Figure 5. Spectrograms of ion differential flux from the (a) LANL 1994-084 satellite and (b) RCM-E simulation. The ratio of RCM-E proton to LANL ion differential flux on a (c) log scale and (d) on a discrete scale in which green, yellow, blue, purple, and red correspond to ratio ranges of [0.5–2], [0.33–0.5] or [2 –5], [0.2–0.33] or [3–5], [0.1–0.2] or [5–10], and <0.1 or >10, respectively.

from the plasma sheet and relatively lower fluxes corresponding to previously trapped plasma that has undergone losses. For illustrative purposes, the black curves in Figures 6a–6f are representative equatorial steady state drift paths of singly charged ions having different first adiabatic invariants for a 50 kV cross-polar cap potential drop (replotted from Figure 11 of *Chen et al.* [1994]). The ions were drifting in an axisymmetric magnetic field model consisting of a uniform southward field $\Delta\mathbf{B}$ added to the geomagnetic dipole field [*Dungey*, 1961] and the Volland-Stern [*Volland*, 1973; *Stern*, 1973] electric field. Superimposed on the plots in Figure 6 are red circles indicating the GEO orbit. The ion kinetic energies at GEO are labeled; these energies range from 10 to 30 keV. At 00:50 MLT at GEO, the steady state drift trajectory plots show direct access from the nightside plasma sheet for all the energies at GEO shown. As the

satellite moves eastward toward dawn along the GEO orbit, it will cross the boundary from open to closed drift paths (for which there is no longer direct access of plasma from the plasma sheet). The plasma there was previously trapped and due to collisional losses presumably has a relatively lower flux than the plasma in the open drift path region. The crossing of the open-closed drift boundary occurs at a later magnetic local time for lower energies, which would explain the dispersion feature in the spectrogram that starts at ~05:10 MLT. As the satellite moves further eastward from dawn to noon, it will cross the boundary from closed to open drift paths, along which there is again direct access from the plasma sheet along open drift paths.

[30] While useful for explaining the general ion dispersion feature in the spectrogram, the illustration in Figure 6 is an idealization corresponding to steady magnetospheric
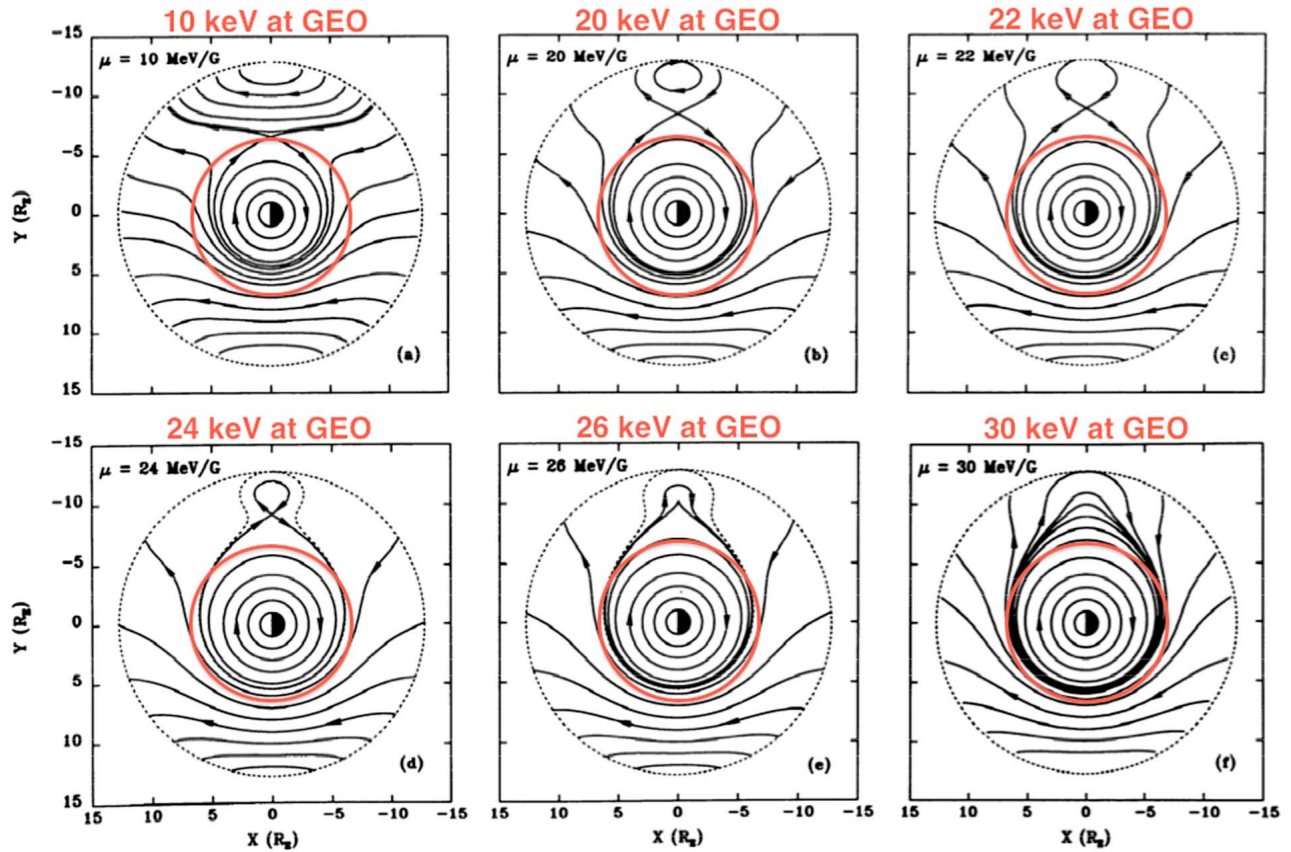
Figure 6. An illustration, taken from *Chen et al.* [1994], of steady state equatorial trajectories of singly charged ions having different first invariant μ values in the equatorial plane for a cross-polar cap potential drop of 50 kV. The red circle indicates the geosynchronous orbit. The energies at GEO are (a) 10 keV, (b) 20 keV, (c) 22 keV, (d) 24 keV, (e) 26 keV, and (f) 30 keV.

magnetic and electric fields [cf. *McIlwain*, 1972]. In reality the electric and magnetic fields were changing with time, and we would expect the open-closed drift path boundaries to vary on short time scales and to become diffuse in the time-averaged configuration. In the spectrogram after about 8:00 MLT, there are several dispersion features. Some of these may correspond to the fluctuations in the magnetic field associated with the sawtooth events.

[31] For comparison with the observed spectrogram in Figure 5a, Figure 5b shows the simulated proton differential flux with the same logarithmic color scale. One can see an ion dispersion feature in the simulated proton flux spectrogram, which looks similar to the observed dispersion feature that starts at ~05:10 MLT. To facilitate comparison of the observed and simulated spectrograms, Figure 5c displays the ratio for the RCM-E proton to LANL 1994-084 ion differential flux on a logarithmic color scale. Figure 5d shows this ratio on a discrete scale in which green, yellow, blue, purple, and red correspond to ratio ranges of [0.5–2], [0.33–0.5] or [2–5], [0.2–0.33] or [3–5], [0.1–0.2] or [5–10], and <0.1 or >10, respectively. This ratio is between 0.5 and 2.0 (see green regions in Figure 5d) over a large range of energies and times. There are large discrepancies at energies above 100 keV, which most likely indicates that the high-energy tail of the boundary spectrum could be specified better. We have already mentioned in section 2.2 that it is difficult to

specify the plasma boundary spectra well from our limited data. There are also some discrepancies at lower energies, which suggest that the model electric field could be improved upon. We will work to include a more realistic estimate of the ionospheric conductance in the RCM-E in future studies. Furthermore, as expected the simulation results do not accurately resolve all the ion dispersion features associated with substorm dipolarizations during this event (see blue regions below 100 keV in Figure 5e) as we do not currently explicitly model dipolarizations. Despite these discrepancies, the overall agreement between the observed and simulated ion differential flux spectra is satisfying. Thus, we find reasonably good simultaneous RCM-E agreement with the magnetic field data and the ion flux data at GEO for this storm event.

[32] We have not yet performed model-data comparisons for the electron flux. Although we have included electron energies up to ~50 keV in our simulations, it would be desirable to extend coverage to electron energies ~500 keV for comparisons with observed ring current electron fluxes. For this we must modify the RCM-E to include a relativistic treatment of electron kinematics. Moreover, a more realistic electron scattering model is needed. Currently the electron loss rate in the RCM-E is everywhere a fraction (=1/3) of the strong pitch angle diffusion rate. Through a simulation-data comparison study, *Chen and Schulz* [2001] showed that
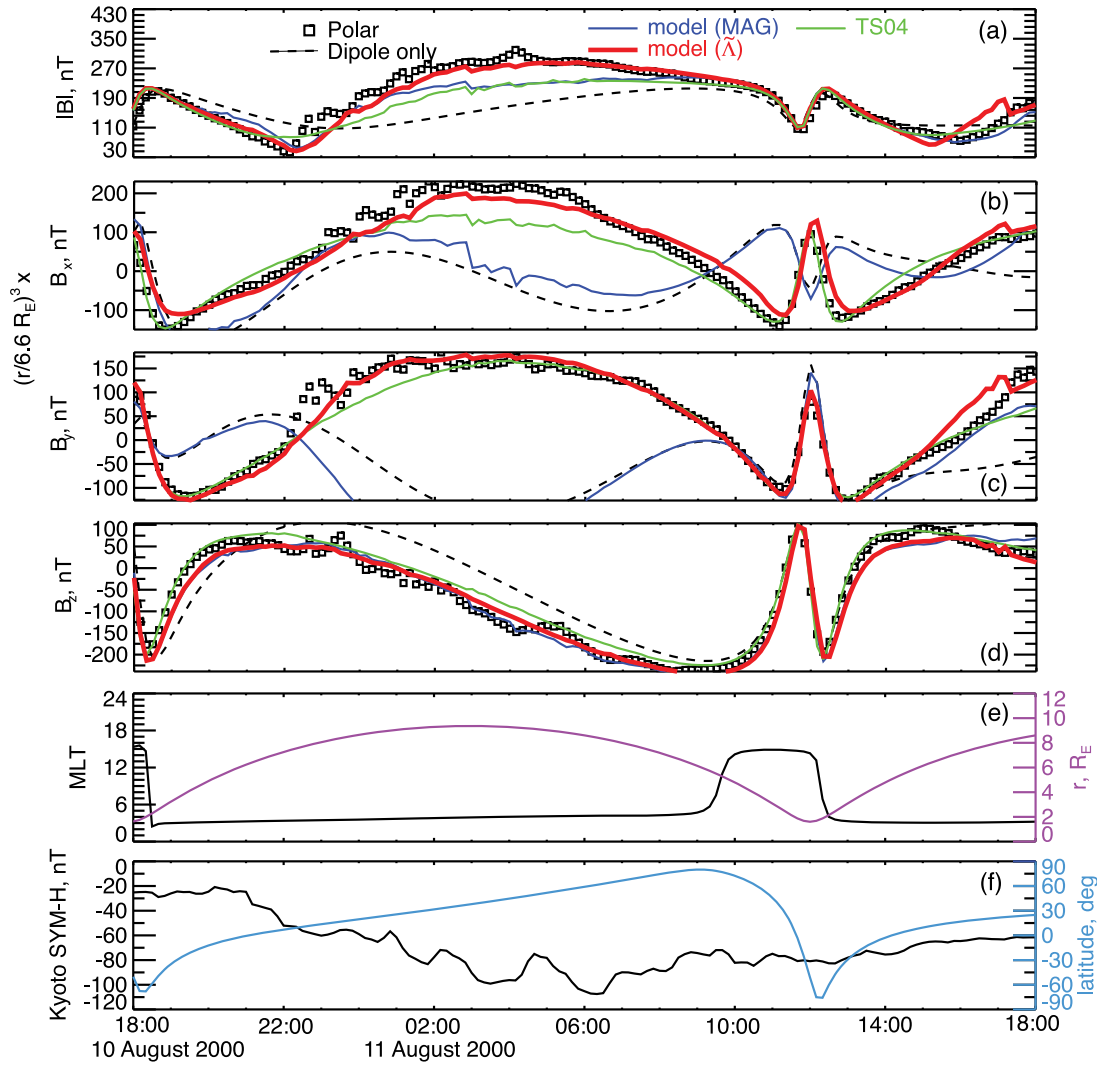
Figure 7. Time traces of the (a) magnetic intensity, (b) B_x, (c) B_y, and (d) B_z. The 10 min averages are given for Polar data (black squares), a dipole field (dashed black curve), the RCM-E in MAG coordinates (blue curve), the RCM-E in Λ coordinates (red curve), and the TS04 model (green curve). (e) The MLT of Polar (black curve) and the dipole tilt (purple curve). (f) The time trace of the Kyoto *SYM-H* index (black curve) and the latitude of Polar (cyan curve).

smoothly MLT-dependent scattering rate is less than strong everywhere, with weakest scattering around 2200 MLT and strongest scattering around 0400 MLT, produces a more realistic electron diffuse aurora than with strong diffusion everywhere.

4.3. Comparisons With Polar Data

[33] Here we perform a similar comparison of the model magnetic field and ion plasma parameters with NASA Polar data. In 2000 the Polar spacecraft was in a highly inclined ($\sim$84° in August 2000) elliptical orbit with a geocentric distance $r = 9\ R_E$ apogee and $r = 1.8\ R_E$ perigee [*Acuña et al.*, 1995]. The black squares in Figure 7 show 10 min averages of magnetic intensity |B| (Figure 7a)and its components from the Polar Magnetic Fields Investigation (MFI) magnetometer (Figures 7b–7d) [*Russell et al.*, 1995]. These values are scaled by a factor of $(r/6.6\ R_E)^3$ in Figure 7 to enable good resolution of the magnetic field data over radial

distances of $r = 1.8$–9 R_E on a linear scale. Figure 7e shows the MLT (black curve) and r (purple curve) of Polar. The *SYM-H* index (black curve) and the magnetic latitude of Polar (cyan curve) are shown in Figure 7f. Figures 7a–7d show that the RCM-E magnetic field values at the $(r, \tilde{\Lambda},$ MLT) coordinates agree best with the Polar magnetic field data. Overall, the appropriately interpreted RCM-E results agree better here with the data than even the empirical TS04 model does.

[34] Next, we compute density n and temperature T from proton spectra provided by the Polar Charge and Mass Magnetospheric Ion Composition Experiment (CAMMICE) [*Fritz et al.*, 1997] and from simulated (RCM-E) proton spectra over energies from 1 to 155 keV. Polar/CAMMICE also measures fluxes of heavy ions such as O^+, but we did not include O^+ ions in our present simulation runs. RCM-E results and CAMMICE data for O^+ during this storm will be
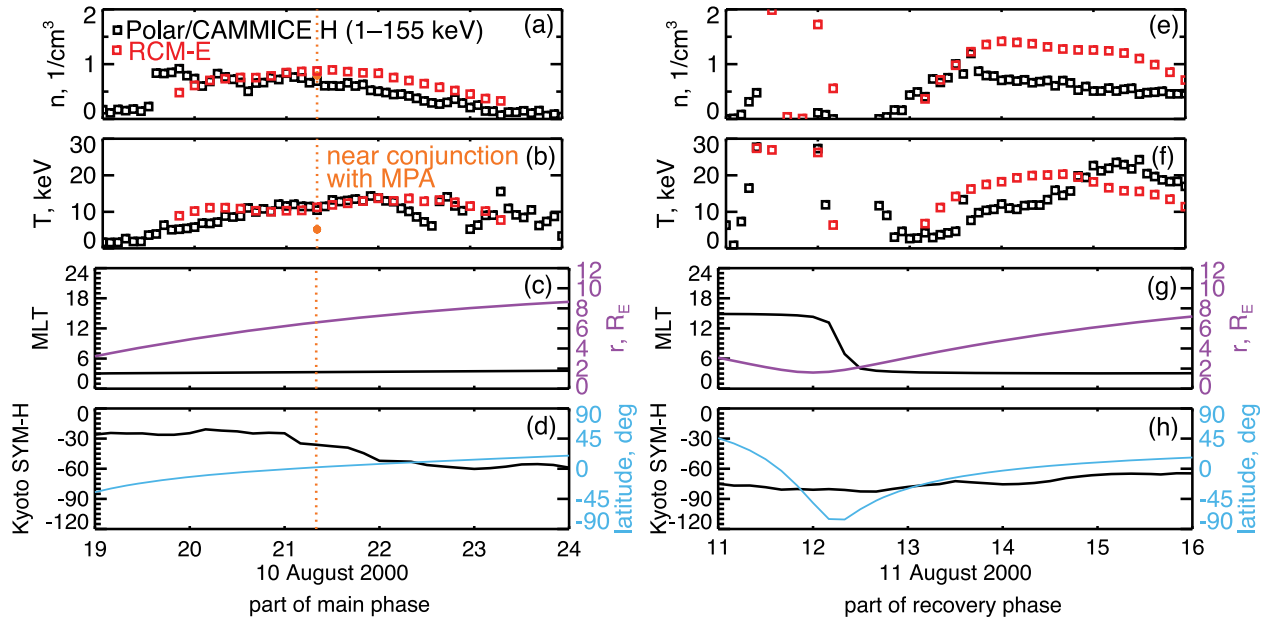
Figure 8. A comparison of (a and e) proton density n and (b and f) temperature T from Polar/CAMMICE (black squares) and RCM-E (red squares). (c and g) The black and purple curves are time histories of the respective geocentric radial distance *r* and MLT of the Polar satellite. (d and h) The blue and black curves show the latitude of Polar and the Kyoto SYM-H index, respectively.

shown elsewhere in the future. We define the proton temperature *T* here as 2/3 of the average proton energy. Ten minute averages of the proton density (Figures 8a and 8d) and temperature (Figures 8b and 8f) from the Polar/CAMMICE data during portions of the main and recovery phases are shown as black squares in Figure 8 (CAMMICE data were not available for 00–11 UT on 11 August 2000). The orange circles in Figures 8a and 8b correspond to LANL/MPA reanalysis values at GEO for the closest conjunction with Polar's orbit near noon. At this near conjunction, the LANL/MPA reanalysis density agrees quite well with the Polar/CAMMICE density. However, the LANL/MPA reanalysis temperature is lower than the Polar/CAMMICE temperature. This discrepancy is expected because the Polar/CAMMICE temperature is calculated from a broader energy range (~1–155 keV) than the ~1 eV to 40 keV range used for estimating temperature from LANL/MPA data. This comparison between the LANL reanalysis and Polar/CAMMICE ion plasma moments provides confidence in the measured plasma moments but reminds us to take account of protons with energies >40 keV in such analyses. The Polar and simulated proton densities and temperatures in Figure 8 agree well during the storm's main phase but not as well (although still within a factor ~2 during the recovery phase). Thus, we find reasonable simultaneous agreement between the observed and simulated (RCM-E) magnetic field and proton plasma moments along Polar's orbit (spanning $r \sim 1.8$–9 R_E) in the magnetosphere during the main phase of this storm event.

5. Summary and Conclusions

[35] In this study we have assessed whether self-consistent RCM-E simulations can account simultaneously for in situ magnetic field and ion flux measurements in the inner magnetosphere ($L \leq 10$) during the large magnetic storm of 10 August 2000. We drove the RCM-E with time-dependent magnetic field, electric field, and plasma boundary conditions that were guided primarily by empirical and assimilative models. Detailed comparisons of the model with observed magnetic field and plasma data were made at GEO and along the orbit of Polar for this storm event. Because the RCM-E does not include the Earth's dipole tilt, we tried two methods for associating the point of observation with coordinates in the RCM-E. One method was to evaluate the RCM-E at the MAG coordinates of the satellite. The new alternative method was to evaluate the RCM-E at the same *r* and MLT as the satellite, but at a magnetic latitude $\tilde{\Lambda}$ equal to the latitudinal separation between the satellite and the surface of minima in B along magnetic field lines in the TS04 model. We found the following results:

[36] 1. The model B_x and B_y did not agree well with the corresponding observed B_x or B_y in MAG coordinates at GEO or along the orbit of Polar. However, the discrepancies between the model B_z and observed B_z in MAG coordinates were smaller than those for the B_x or B_y.

[37] 2. The model B_x, B_y, and B_z in the $(r, \tilde{\Lambda}, MLT)$ coordinates agreed reasonably well with the corresponding observations at GEO ($r = 6.6$ R_E) and along the orbit of Polar ($r \sim 1.8$–9 R_E). In some cases, notably throughout the main phase of the 10–11 August 2000 storm, agreement was even better than the agreement between TS04 and observed magnetic fields.

[38] 3. Our simulations did not reproduce sawtooth fluctuations in the observed magnetic field. These are thought to be associated with substorm dipolarizations [e.g., *Henderson et al.*, 2006], but we did not explicitly include the effects of substorm dipolarizations in our RCM-E simulations.

[39] 4. The RCM-E did well at reproducing prominent observed ion dispersion features in the LANL 1994-084 ion differential flux spectra over energies ∼1–150 keV at GEO.

[40] 5. The simulated and Polar/CAMMICE proton density n and temperature T over energies of ∼1–155 keV agreed well with each other during the main phase of the storm event.

[41] 6. Despite uncertainties in the magnetic field, electric field and plasma boundary conditions, the self-consistent RCM-E simulations appear to account simultaneously for in situ magnetic field and ion flux measurements for the large 10 August 2000 storm.

[42] It is very encouraging to find that self-consistent simulations can simultaneously account for in situ magnetic field and proton flux measurements in the inner magnetosphere for the large storm event of 10–11 August 2000. However, we still need to follow up with model-data comparisons for typically less dominant, but still important contributors to the ring current energy content such as O^+ ions and electrons.

References

Acuña, M. H., K. W. Ogilvie, D. N. Baker, S. A. Curtis, D. H. Fairfield, and W. H. Mish (1995), The Global Geospace Science program and its investigations, *Space Sci. Rev.*, 71, 5–21, doi:10.1007/BF00751323.

Belian, R. D., et al. (1992), High-*Z* energetic particles at geosynchronous orbit during the great solar proton event series of October 1989, *J. Geophys. Res.*, 97(A11), 16,897–16,906, doi:10.1029/92JA01139.

Bilitza, D., and B. W. Reinisch (2008), International Reference Ionosphere 2007: Improvements and new parameters, *J. Adv. Space Res.*, 42(4), 599–609, doi:10.1016/j.asr.2007.07.048.

Borovsky, J. E., M. F. Thomsen, and D. J. McComas (1997), The superdense plasma sheet: Plasmaspheric origin, solar wind origin, or ionospheric origin?, *J. Geophys. Res.*, 102(A10), 22,089–22,097, doi:10.1029/96JA02469.

Cahill, L. J. (1966), Inflation of the inner magnetosphere during a magnetic storm, *J. Geophys. Res.*, 71(19), 4505–4519, doi:10.1029/JZ071i019p04505.

Chen, M. W., and M. Schulz (2001), Simulations of diffuse aurora with plasma sheet electrons in pitch angle diffusion less than everywhere strong, *J. Geophys. Res.*, 106(A12), 28,949–28,966, doi:10.1029/2001JA000138.

Chen, M. W., M. Schulz, and L. R. Lyons (1994), Simulations of phase space distributions of stormtime proton ring current, *J. Geophys. Res.*, 99(A4), 5745–5759, doi:10.1029/93JA02771.

Chen, M. W., M. Schulz, S. Liu, G. Lu, L. R. Lyons, M. El-Alaoui, and M. Thomsen (2005), Simulated stormtime ring-current magnetic field produced by ions and electrons, in *Inner Magnetosphere Interactions: New Perspective From Imaging*, Geophys. Monogr. Ser., vol. 159, edited by J. Burch, M. Schulz, and H. Spence, pp. 237–250, AGU, Washington, D. C., doi:10.1029/159GM18.

Chen, M. W., S. Liu, M. Schulz, J. L. Roeder, and L. R. Lyons (2006), Magnetically self-consistent ring current simulations during the 19

October 1998 storm, *J. Geophys. Res.*, 111, A11S15, doi:10.1029/2006JA011620.

Chen, M. W., C.-P. Wang, M. Schulz, and L. R. Lyons (2007), Solar-wind influence on MLT dependence of plasmasheet conditions and their effects on stormtime ring current formation, *Geophys. Res. Lett.*, 34, L14112, doi:10.1029/2007GL030189.

Christon, S. P., D. J. Williams, D. G. Mitchell, C. Y. Huang, and L. A. Frank (1991), Spectral characteristics of plasma sheet ion and electron populations during disturbed geomagnetic conditions, *J. Geophys. Res.*, 96(A1), 1–22, doi:10.1029/90JA01633.

de Gonzalez, A. L. C., and W. D. Gonzalez (1998), Analytical study of the energy rate balance equation for the magnetospheric storm-ring current, *Ann. Geophys.*, 16, 1445–1454.

Dessler, A. J., and E. N. Parker (1959), Hydromagnetic theory of geomagnetic storms, *J. Geophys. Res.*, 64(12), 2239–2252, doi:10.1029/JZ064i012p02239.

Dungey, J. W. (1961), Interplanetary magnetic field and the auroral zones, *Phys. Rev. Lett.*, 6, 47–48, doi:10.1103/PhysRevLett.6.47.

Fok, M.-C., T. Moore, and M. Greenspan (1996), Ring current development during storm main phase, *J. Geophys. Res.*, 101(A7), 15,311–15,322, doi:10.1029/96JA01274.

Frank, L. A. (1967), On the extraterrestrial ring current during geomagnetic storms, *J. Geophys. Res.*, 72(15), 3753–3767, doi:10.1029/JZ072i015p03753.

Fritz, T. A., I. A. Daglis, S. Livi, H. Sommer, B. Wilken, M. Grande, D. D. Hall, J. B. Blake, J. F. Fennell, and R. Koga (1997), The POLAR CAMMICE investigation, technical report, Cent. for Space Phys., Boston, Mass.

Gradshteyn, I. S., and I. M. Ryzhik (1980), *Table of Integrals, Series, and Products*, translated from Russian by A. Jeffrey, 292 pp., Academic, New York.

Henderson, M. G., et al. (2006), Substorms during the 10–11 August 2000 sawtooth event, *J. Geophys. Res.*, 111, A06206, doi:10.1029/2005JA011366.

Jordanova, V. K., C. J. Farrugia, L. Janoo, J. M. Quinn, R. B. Torbert, K. W. Ogilvie, R. P. Lepping, J. T. Steinberg, D. J. McComas, and R. D. Belian (1998), October 1995 magnetic cloud and accompanying storm activity: Ring current evolution, *J. Geophys. Res.*, 103(A1), 79–92, doi:10.1029/97JA02367.

Jordanova, V. K., Y. S. Miyoshi, S. Zaharia, M. F. Thomsen, G. D. Reeves, D. S. Evans, C. G. Mouikis, and J. F. Fennell (2006), Kinetic simulations of ring current evolution during the Geospace Environment Modeling challenge events, *J. Geophys. Res.*, 111, A11S10, doi:10.1029/2006JA011644.

Kihn, E. A., and A. J. Ridley (2005), A statistical analysis of the assimilative mapping of ionospheric electrodynamics auroral specification, *J. Geophys. Res.*, 110, A07305, doi:10.1029/2003JA010371.

Kozyra, J. U., V. K. Jordanova, J. E. Borovsky, M. F. Thomsen, D. J. Knipp, D. S. Evans, D. J. McComas, and T. E. Cayton (1998), Effects of a high-density plasma sheet on ring current development during the November 2–6, 1993, magnetic storm, *J. Geophys. Res.*, 103(A11), 26,285–26,305, doi:10.1029/98JA01964.

Lavraud, B., and V. K. Jordanova (2007), Modeling the effects of cold-dense and hot-tenuous plasma sheet on proton ring current energy and peak location, *Geophys. Res. Lett.*, 34, L02102, doi:10.1029/2006GL027566.

Lemon, C. L. (2005), Simulating the driven magnetosphere, PhD thesis, Rice Univ., Houston, Tex.

Lemon, C., F. Toffoletto, M. Hesse, and J. Birn (2003), Computing magnetospheric force equilibria, *J. Geophys. Res.*, 108(A6), 1237, doi:10.1029/2002JA009702.

Lemon, C., R. Wolf, T. W. Hill, and S. Sazykin (2004), Magnetic storm ring current injection modeled with the Rice Convection Model and a self-consistent magnetic field, *Geophys. Res. Lett.*, 31, L21801, doi:10.1029/2004GL020914.

Liemohn, M. W. (2003), Yet another caveat to using the Dessler–Parker–Sckopke relation, *J. Geophys. Res.*, 108(A6), 1251, doi:10.1029/2003JA009839.

Liemohn, M. W., J. U. Kozyra, M. F. Thomsen, J. L. Roeder, G. Lu, J. E. Borovsky, and T. E. Cayton (2001), Dominant role of the asymmetric ring current in producing the stormtime *Dst**, *J. Geophys. Res.*, 106(A6), 10,883–10,904, doi:10.1029/2000JA000326.

Liu, S., M. W. Chen, M. Schulz, and L. R. Lyons (2006), Initial simulation results of storm-time ring current in a self-consistent magnetic field model, *J. Geophys. Res.*, 111, A04225, doi:10.1029/2005JA011194.

McComas, D. J., S. J. Bame, B. L. Barraclough, J. R. Donart, R. C. Elphic, J. T. Gosling, M. B. Moldwin, K. R. Moore, and M. F. Thomsen (1993), Magnetospheric plasma analyzer: Initial 3-spacecraft observations

from geosynchronous orbit, *J. Geophys. Res.*, *98*(A8), 13,453–13,465, doi:10.1029/93JA00726.

McIlwain, C. E. (1972), Plasma convection in the vicinity of the geosynchronous orbit, in *Earth's Magnetospheric Processes*, edited by B. M. McCormac, pp. 268–279, D. Reidel, Norwell, Mass., doi:10.1007/978-94-010-2896-7_27.

Mead, G. D. (1964), Deformation of the geomagnetic field by the solar wind, *J. Geophys. Res.*, *69*(7), 1181–1195, doi:10.1029/JZ069i007p01181.

Nakada, M. P., J. W. Dungey, and W. N. Hess (1965), On the origin of outer-belt protons: 1, *J. Geophys. Res.*, *70*(15), 3529–3532, doi:10.1029/JZ070i015p03529.

O'Brien, T. P., and C. L. Lemon (2007), Reanalysis of plasma measurements at geosynchronous orbit, *Space Weather*, *5*, S03007, doi:10.1029/2006SW000279.

Richmond, A. D., G. Lu, B. A. Emery, and D. J. Knipp (1998), The AMIE procedure: Prospects for space weather specification and prediction, *Adv. Space Res.*, *22*, 103–112, doi:10.1016/S0273-1177(97)01108-3.

Roederer, J. G., H. H. Hilton, and M. Schulz (1973), Drift shell splitting by internal geomagnetic multipoles, *J. Geophys. Res.*, *78*(1), 133–144, doi:10.1029/JA078i001p00133.

Russell, C. T. (1971), Geophysical coordinate transformations, *Cosmic Electrodyn.*, *2*, 184–196.

Russell, C. T., R. C. Snare, J. D. Means, D. Peirce, D. Dearborn, M. Larson, G. Barr, and G. Le (1995), The GGS/POLAR magnetic fields investigation, *Space Sci. Rev.*, *71*, 563–582, doi:10.1007/BF00751341.

Sckopke, N. (1966), A general relation between the energy of trapped particles and the disturbance field near the Earth, *J. Geophys. Res.*, *71*(13), 3125–3130, doi:10.1029/JZ071i013p03125.

Shabansky, V. P. (1971), Some processes in the magnetosphere, *Space Sci. Rev.*, *12*(3), 299–418, doi:10.1007/BF00165511.

Stern, D. P. (1973), A study of the electric field in an open magnetospheric model, *J. Geophys. Res.*, *78*(31), 7292–7305, doi:10.1029/JA078i031p07292.

Toffoletto, F. R., R. W. Spiro, R. A. Wolf, J. Birn, and M. Hesse (2000), Computer experiments on substorm growth and expansion, in *Proceedings of the 5th International Conference on Substorms, St. Petersburg, Russia, 16–20 May 2000, Eur. Space Agency Spec. Publ.*, ESA SP-443, 351–355.

Toffoletto, F. R., R. W. Spiro, R. A. Wolf, J. Birn, and M. Hesse (2001), Modeling inner magnetospheric electrodynamics, in *Space Weather, Geophys. Monogr. Ser.*, vol. 125, edited by P. Song, H. J. Singer, and G. L. Siscoe, pp. 265–272, AGU, Washington, D. C., doi:10.1029/GM125p0265.

Toffoletto, F., S. Sazykin, R. Spiro, R. Wolf (2003), Inner magnetospheric modeling with the Rice Convection Model, *Space Sci. Rev.*, *107*(1–2), 175–196.

Tsyganenko, N. A. (2002a), A model of the near magnetosphere with a dawn-dusk asymmetry: 1. Mathematical structure, *J. Geophys. Res.*, *107*(A8), 1179, doi:10.1029/2001JA000219.

Tsyganenko, N. A. (2002b), A model of the near magnetosphere with a dawn-dusk asymmetry: 2. Parameterization and fitting to observations, *J. Geophys. Res.*, *107*(A8), 1176, doi:10.1029/2001JA000220.

Tsyganenko, N. A., and M. I. Sitnov (2005), Modeling the dynamics of the inner magnetosphere during strong geomagnetic storms, *J. Geophys. Res.*, *110*, A03208, doi:10.1029/2004JA010798.

Volland, H. (1973), A semiempirical model of large-scale magnetospheric electric fields, *J. Geophys. Res.*, *78*(1), 171–180, doi:10.1029/JA078i001p00171.

Williams, D. J. (1981), Phase space variations of near equatorially mirroring ring current ions, *J. Geophys. Res.*, *86*(A1), 189–194, doi:10.1029/JA086iA01p00189.

Wygant, J., D. Rowland, H. Singer, M. Temerin, and M. K. Hudson (1998), Experimental evidence on the role of the large spatial scale electric field in creating the ring current, *J. Geophys. Res.*, *103*(A12), 29,527–29,544, doi:10.1029/98JA01436.

Yang, J., F. R. Toffoletto, and Y. Song (2010), Role of depleted flux tubes in steady magnetospheric convection: Results of RCM-E simulations, *J. Geophys. Res.*, *115*, A00I11, doi:10.1029/2010JA015731.

Yu, Y., V. Jordanova, S. Zaharia, J. Koller, J. Zhang, and L. M. Kistler (2012), Validation study of the magnetically self-consistent inner magnetosphere model RAM-SCB, *J. Geophys. Res.*, *117*, A03222, doi:10.1029/2011JA017321.

Zaharia, S., V. K. Jordanova, M. F. Thomsen, and G. D. Reeves (2006), Self-consistent modeling of magnetic fields and plasma in the inner magnetospehre: Application to a geomagnetic storm, *J. Geophys. Res.*, *111*, A11S14, doi:10.1029/2006JA011619.

Zaharia, S., V. K. Jordanova, D. Welling, and G. Tóth (2010), Self-consistent inner magnetosphere simulation driven by a global MHD model, *J. Geophys. Res.*, *115*, A12228, doi:10.1029/2010JA015915.